Pre-print:
M. Ciofalo, M. La Cerva, M. Di Liberto, L. Gurreri, A. Cipollina, G. Micale, *Optimization of net power density in Reverse Electrodialysis*, Energy, 181 (2019) 576–588, https://doi.org/10.1016/j.energy.2019.05.183

Optimization of net power density in Reverse Electrodialysis

Michele Ciofalo*, Mariagiorgia La Cerva, Massimiliano Di Liberto,
Luigi Gurreri, Andrea Cipollina, Giorgio Micale
Dipartimento dell'Innovazione Industriale e Digitale (DIID)
Università degli Studi di Palermo, Palermo, Italy

ABSTRACT

Reverse Electrodialysis (RED) extracts electrical energy from the salinity difference between two solutions using selective ion exchange membranes. In RED, the conditions yielding the largest net power density (*NPD*) are often close to those yielding the minimum unitary cost of the electrical energy produced, due to the still large cost of the membranes. *NPD* depends on a large number of physical and geometric parameters. Some of these can be regarded as "scenario" variables, imposed by external constraints (e.g., availability) or chosen by different criteria than *NPD* maximization. Others, among which the thicknesses H^{CONC}, H^{DIL} and the velocities U^{CONC}, U^{DIL} in the concentrate and diluate channels, have contrasting effects, so that the *NPD* maximum is obtained for some intermediate values of these variables.

In the present study, a simplified model of a RED stack was coupled with an optimization algorithm in order to determine the conditions of maximum *NPD* in the space of the variables H^{CONC}, H^{DIL},U^{CONC}, U^{DIL} for different sets of "scenario" variables. The model accounts for entrance effects, property variation, concentration polarization, axial concentration changes, osmotic, electro-osmotic and diffusive fluxes. Although it is essentially one-dimensional, it can deal with complex (e.g., spacer-filled) channel geometries using friction factors, mass transfer coefficients and Ohmic resistances computed by 3-D simulations. The study shows that an optimal choice of the free design parameters for any given scenario, as opposed to the adoption of standard fixed values, may provide significant improvements in *NPD*.

KEYWORDS

Reverse electrodialysis; net power density; salinity gradient; optimization; gradient ascent

* Corresponding author; e-mail: michele.ciofalo@unipa.it

1. Introduction

Reverse ElectroDialysis (RED) is an electromembrane process harvesting electrical energy from the salinity gradient between two solutions. Several repeating elements, or cell pairs (from a few at lab-scale [1, 2] to some hundreds in industrial units [3]) are stacked in a plate-and-frame configuration, Figure 1(a). Each cell pair, Figure 1(b), includes an anion exchange membrane (*AEM*), a concentrate channel (*CONC*), a cation exchange membrane (*CEM*), and a diluate channel (*DIL*), for a total thickness H_{CP} typically < 1 mm. The channels through which the solutions flow can be 100-300 μm thick and are usually created by spacers, although self-distancing profiled membranes have also been proposed [4-6]. The feed flow velocity is of the order of 1 cm/s.

The end compartments in Figure 1(a) contain red-ox solutions which convert the ion flux into an electron flux [7], and are delimited by continuous or segmented electrodes which can be closed on a resistive load R_{LOAD} *via* an external circuit. For any value of R_{LOAD}, the net power which can be provided by a RED stack depends upon theoretical maximum electromotive force (ideal open circuit voltage); Ohmic losses; non-Ohmic phenomena; and pumping power consumption [8].

The ideal open circuit voltage depends only on the ratio between the ions activities in the two feed solutions and on the permselectivity of the membranes. This last parameter is close to 1 in dilute solutions, but can decrease significantly when concentrated solutions are adopted [9].

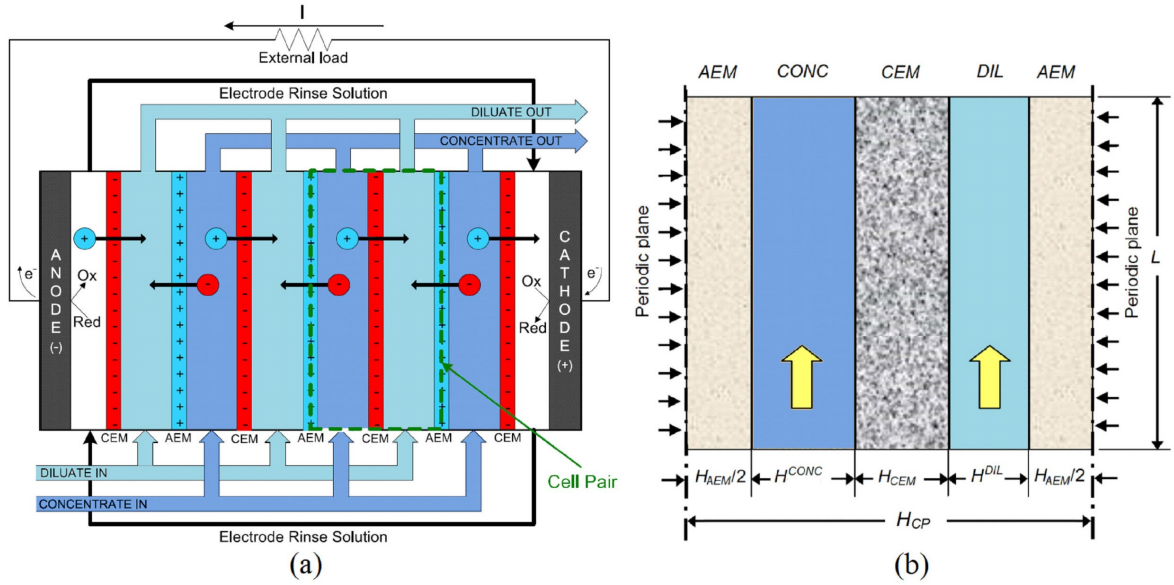

Figure 1. Schematic representation of a RED stack (a) and of an individual cell pair (b) (adapted from [10]).

Ohmic losses η_{Ω} arise in all stack elements (membranes, solutions and electrode compartments). When a low concentration solution such as riverwater is fed to the diluate channels, these latter give the main contribution to Ohmic resistance [11]; conversely, the membranes' resistance is dominant when more concentrated solutions are used [10]. Spacers, being non-conductive, cause an increase of the compartment's Ohmic resistance; under this respect, profiled membranes may be preferable.

The ion transport from the concentrate to the diluate channel causes concentration changes resulting in a reduction of driving force and thus in a further voltage drop. This can be split into two contributions, respectively associated with: (i) the axial concentration change in the bulk of the solution ($\eta_{\Delta C}$), and (ii) the transverse concentration change across the diffusion boundary layers (η_{BL}). The terms $\eta_{\Delta C}$ and η_{BL} are often collectively called "non-Ohmic losses" [12].

In regard to $\eta_{\Delta C}$, in an ideal stack it depends only on Coulombic ion fluxes proportional to the current density, but in real stacks also osmotic and electro-osmotic fluxes of water and diffusive fluxes of co-ions through the membranes contribute to $\eta_{\Delta C}$ [13, 14]. If the seawater–riverwater couple is used, $\eta_{\Delta C}$ is comparable with the Ohmic voltage drop [4, 9].

In regard to η_{BL}, when an electrical current flows through the stack, concentration boundary layers develop between the fluid bulk and the membrane surfaces [13] and reduce the available driving force [15]. This phenomenon is known as *concentration polarization.* If the seawater–riverwater couple is used, the contribution of η_{BL} to the stack resistance may be significant [4, 16], though generally lower than axial and Ohmic voltage drops. The term η_{BL} depends strongly on mixing, and thus on channel geometry (size and shape) and flow rate [17]; it decreases for decreasing channel thickness [18] and can be reduced by spacers [19]. Both $\eta_{\Delta C}$ and η_{BL} may become negligible for highly concentrated solutions [9, 17].

When natural solutions are used, the stack performance may be significantly reduced by the effects of di-valent ions on membrane resistance and permselectivity [20]. However, most models neglect such effects.

Finally, the net power may significantly be reduced by the energy spent for pumping the feed solutions. At the flow rate that maximizes the net power, this reduction is typically ~10-20% when net spacers are used [1, 4, 17, 18]. Manifolds and external piping also contribute to pumping losses [21].

The optimization of RED systems is crucial for the promotion of the technology readiness level. However, only few studies have been carried out so far. Veerman *et al*. [22] developed for the first time a one-dimensional process model requiring empirical membrane

properties. The model was based on some simplifying assumptions, e.g. independence of membranes' resistance on the solutions' concentrations and negligible concentration polarization effects. Moreover, pressure drops were calculated using experimental information. Channels' thicknesses and flow rates were optimized for different stack lengths in order to explore the different scenarios arising from three response parameters: the net power density, the net energy density and the quantity given by their product.

The same general approach of simulation was adopted in some recently published optimization studies [23-25], which include also other parameters in the objective functions, i.e. the lost work (with respect to the total energy from complete mixing) and the energy efficiency. Long *et al*. [24] simulated stacks with 50 cell pairs, 10×10 cm^2 active area and 200 μm thick channels, fed by seawater and river water solutions. Different membranes were simulated, thus finding the optimal flow velocities for each stack. The optimization was first conducted with the single objectives of maximum net power density and maximum energy efficiency. Then, a multi-objective optimization was performed taking into account both parameters and changing their weights. An algorithm selected the optimal point for each membrane stack. In another work [25], the same authors found optimal values of flow rates and channels' thicknesses in stacks of given sizes, including the total thickness, fed by seawater and river water solutions. Again, stacks made by different membranes were simulated. However, in this case, only the net power density was maximized.

Simulation results from the studies on RED optimization showed that optimal values may change significantly with the selected optimization criterion. Moreover, the above short review of pertinent literature shows that there is an intrinsic level of arbitrariness in the choice of the objective function, as well as in the assignment of the weights in the case of multi-objective analyses. Rather, the economic assessment is needed for a complete optimization study, i.e. aimed at finding the minimum cost of the energy produced. In this sense, given the high cost of the ion exchange membranes, the maximization of the net power density can be regarded as a reliable optimization objective, which provides useful insights on system designs oriented to the cost reduction.

Starting from the modelling approach by Veerman *et al*. [1], we have developed a process model enriched by several implementations [10]. Correlations of physical properties suitable also for concentrated brines have been adopted, in order to adapt the model capabilities also for the simulation of RED applications in specific sites as saltworks [3, 26] and in closed-loops [27, 28]. The dependence of membranes' resistance on the solutions' concentrations has been included, and concentration polarization effects on the membrane potential have been accounted for. Moreover, fluid dynamics and mass transfer have been characterized by CFD

simulation, which provides basic information on pressure drop and concentration polarization.

In this work, we used our RED model [10] for an optimization study of broader range and from a different perspective with respect to the few examples available in the literature. The maximum net power density per cell pair has been searched for a single membrane type, analysing the effects of several operating and constructing parameters: inlet flow velocities and concentrations, channels' thicknesses, stack length, flow arrangement (parallel or counter-flow). Moreover, ideal spacer-less channels and channels filled by a woven net spacer were simulated.

2. Model

2.1. Basic assumptions

The model used in the present paper is based on the so called "segmented" approach, in which the potential difference across the external load is obtained by subtracting from the open circuit voltage a number of voltage drop terms which account for the above mentioned polarization and Ohmic effects. Axial concentration profiles are computed from mass balance equations accounting for non-ideal phenomena such as osmotic and electro-osmotic fluxes and diffusion in the membranes. The model uses a one-dimensional representation of the stack but complements it with local results (friction coefficients, mass transfer coefficients, and Ohmic resistances) computed by a fully 3-D approach. This combined treatment is similar to that adopted by Pawlowski *et al*. [29].

A detailed description of the model has been given in a previous paper [10] and will not be repeated here. The model was implemented on different platforms including G95 Fortran. It was validated by comparison with measurements of the gross power density (*GPD*) as a function of the flow velocity presented by Veerman *et al*. [1] and with measurements of *GPD* as a function of the total current presented by Choi *et al.* [30].

2.2. Typical results

The following Figures 2-5 illustrate the typical results that the model can provide. Figure 2 reports axial profiles of the electric potentials (per cell pair) along the streamwise coordinate *y* (orientated as the concentrated solution velocity) for an arbitrary parallel flow configuration and a potential difference across the external load v_{LOAD}=0.06 V (per cell pair).

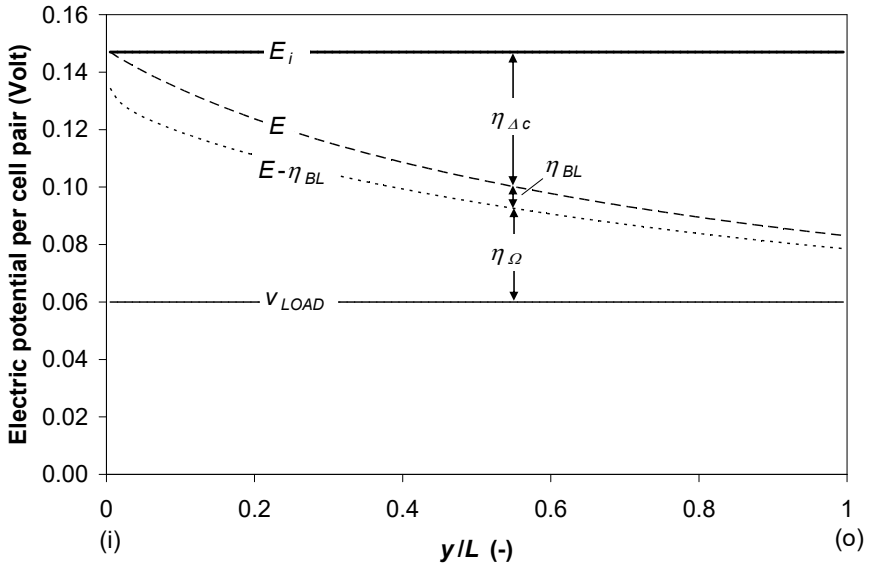

Figure 2. Electric potentials per cell pair. *i*=inlet, *o*=outlet, *y*=flow direction, *E*= electromotive force, $\eta_{\Delta c}$=voltage drop due to concentration changes along *y*, η_{BL}=voltage drop due to concentration polarization, $\eta_{\Omega}=i(r_{\Omega}+r_{blank})$=Ohmic voltage loss, v_{LOAD}=electric potential difference across the external load divided by the number of cell pairs.

Note that, over most of the stack length, the largest potential drops are those due to axial concentration variations ($\eta_{\Delta C}$) and Ohmic losses (η_{Ω}). As *y* increases, $\eta_{\Delta C}$ increases while η_{Ω} decreases. Non-Ohmic losses associated with concentration polarization (η_{BL}) are comparable with the other losses only in the first region of the stack, and play a secondary role elsewhere.

The model computes also axial profiles of bulk concentrations; as *y* increases, these tend asymptotically to two values C_{∞}^{CONC}, C_{∞}^{DIL}, such that the associated electromotive force *E* equals the potential difference v_{LOAD} imposed between the electrodes, and the local current density *i* and Ohmic losses η_{Ω} vanish. For realistic stack lengths, this condition is usually far from being reached. Finally, the model yields axial profiles of the local current density *i*. This initially increases due to the decreasing Ohmic resistivity of the dilute solution, and then decreases exponentially. Examples of all these axial profiles are shown in ref. [10].

By letting the potential difference v_{LOAD} between the electrodes increase from zero in small steps (e.g. 0.001 V), current-voltage characteristic curves like those reported in Figure 3 are obtained.

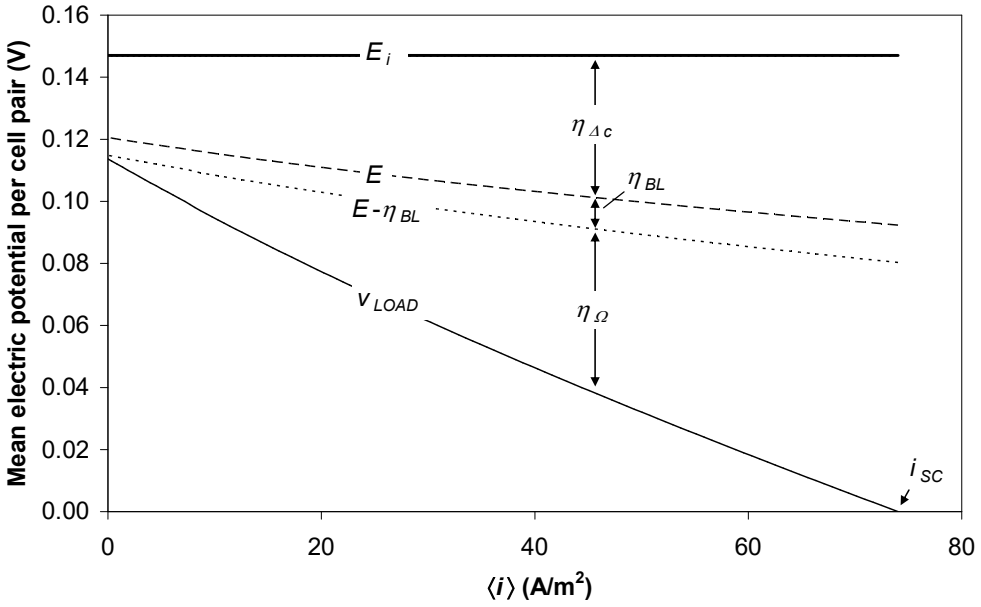

Figure 3. Typical results of the model: current density-voltage characteristic curves.

Here, voltage drops and current density $\langle i \rangle$ are averaged over the stack length L (i.e., over the stack projected surface $S=LW$). Note that the electromotive force at inlet, E_i (~0.147 V), equal to the ideal open circuit voltage, as well as the potential difference v_{LOAD} across the external load r_{LOAD}, are uniform along the stack and thus do not have to be averaged. By i_{SC} we denote the short circuit current density corresponding to $r_{LOAD}=0$ and $v_{LOAD}=0$ (~74 A/m^2 in the present example). Note that, under open circuit conditions ($\langle i \rangle=0$), the axial voltage drop $\eta_{\Delta C}$ would vanish only in an ideal stack, i.e. in the absence of non-ideal effects (osmotic and electro-osmotic water flux and diffusive salt flux), but is significant in a real stack such as that considered here. For $\langle i \rangle=0$ also polarization losses η_{BL} would vanish under ideal conditions, but are non-zero here due to the diffusive salt flux. As a consequence, the voltage across the load per cell pair (v_{LOAD}) under open circuit conditions ($r_{LOAD} \to \infty$), which would be equal to 0.147 V in an ideal stack, is only ~0.12 V in the present, real conditions. Only the Ohmic loss η_{Ω} vanishes under open circuit conditions both in an ideal stack and in a real one.

The diagram in Figure 3, which is for a single cell pair and per unit area, can be turned into a *V-I* (total voltage – total current) plot (Figure 4) by multiplying v_{LOAD} by n_{CP} (number of cell pairs in the stack) and $\langle i \rangle$ by $S=L \cdot W$ (projected surface area of the stack, L being the stack length and W its spanwise width). For any given external load R_{LOAD} the intersection of the resulting $V(I)$ curve (internal characteristic) with the straight line of slope R_{LOAD} (external characteristic) determines the working point P.

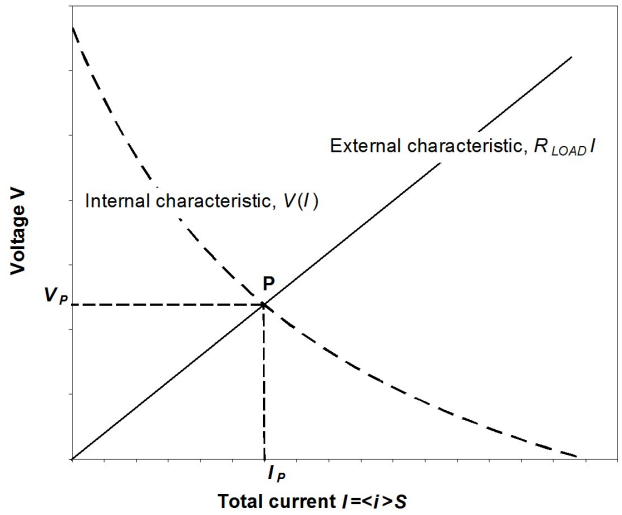

Figure 4. Internal and external characteristics and working point P (schematic).

For example, for the reference case considered in Figure 3 and a stack with n_{CP}=100 and S=0.16 m^2 (L=W=0.4 m), the internal characteristic would decrease from 0.12×100 =12 V for I=0 (open circuit) to 0 for I=i_S×S=11.84 A (short circuit). For a load resistance R_{LOAD} of 1 Ω the working point would be at I_P≈6 A, V_P≈5 V, yielding a gross electrical power of ~30 W.

For the same example considered in Figure 3, Figure 5 reports the corresponding power density curves (per cell pair) as functions of the average current density ⟨i⟩. It also reports the net power density (per cell pair) *NPD*=*GPD*-*PPD*. Due to non-Ohmic effects, the maximum gross power density *GPD* is attained for a mean current density ⟨i⟩ slightly less than i_S/2. The same value of ⟨i⟩ maximizes also the net power density *NPD* since the pumping power density *PPD* does not depend on ⟨i⟩. Under the conditions assumed in this example, pumping losses are a small fraction of the gross power density.

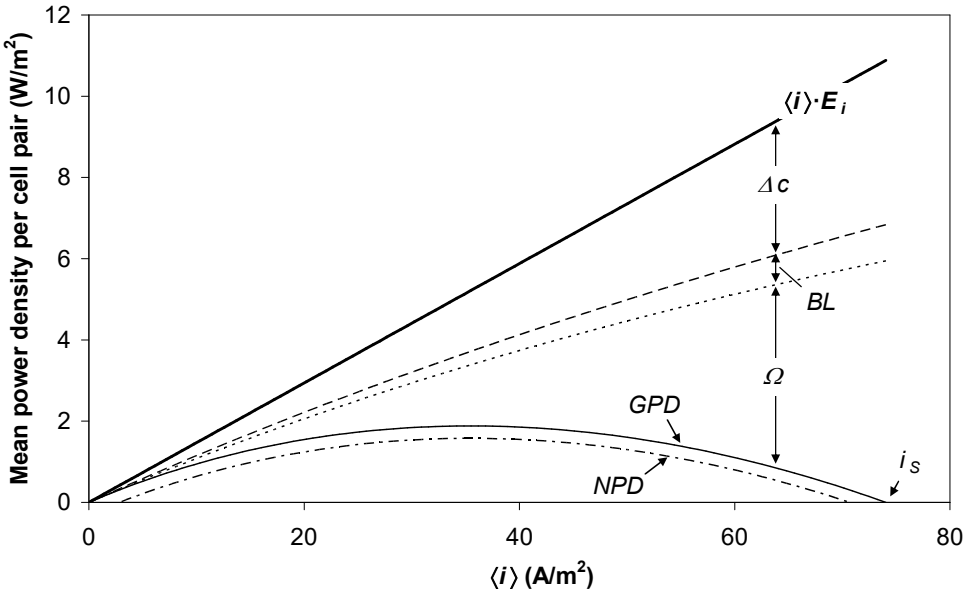

Figure 5. Typical results of the model: current density-power density curves.

3. Optimization study

3.1. Optimization and "scenario" variables

From the above model description there follows that *NPD* and all other performance parameters of a given RED stack are functions of several variables. They have been listed in Table 1, grouped by type.

Note that Table 1 does not include either physical constants (e.g. the gas constant R_G or the Faraday constant F) or quantities that, at least under the present modelling assumptions, have no influence on the stack performance, such as the stack width W and the number of cell pairs n_{CP} (provided all quantities are referred to the single cell pair).

Now, some of the listed variables are not at the designer's disposal, but are imposed by availability considerations (e.g. electrolyte nature, T, C_i^{CONC} and C_i^{DIL}, at least in "open" RED in which concentrate and dilute solutions are naturally available). Others exert a monotonic influence, either beneficial or detrimental, on *NPD*: for example, singular pressure loss coefficients reduce *NPD* and should be made as low as possible; similarly, the blank resistance r_{blank} of the electrode compartments reduces *NPD* and should be kept to a minimum. The above quantities need not to be included in an optimization study, but can be regarded as "scenario" variables whose values are dictated by availability, design, economical or technological considerations other than the purpose of maximizing *NPD*.

On the other hand, some variables, namely, the thicknesses H^{CONC}, H^{DIL} and the inlet

velocities U_i^{CONC}, U_i^{DIL} in the concentrate and dilute channels, are at the designer's disposal and exert contrasting effects, so that an *NPD* maximum is obtained for intermediate values of these parameters.

Table 1. Variables affecting the net power density (NPD) in Reverse Electrodialysis

a) Design parameters and operating conditions

Quantity	*Symbol*	*Reference value or range*
Electrolyte nature (with associated physical properties and hydration number n_H)	-	NaCl (n_H=7)
Inlet concentrations	C_i^{CONC}, C_i^{DIL}	"Scenario" variables (500-5000 and 5-100 mol/m^3, respectively)
Channel thickness	H^{CONC}, H^{DIL}	Both 200 μm
Inlet velocities	U_i^{CONC}, U_i^{DIL}	Both 2 cm/s
Stack length	L	"Scenario variable (0.1-1 m)
Flow arrangement	-	"Scenario variable (parallel flow or counter flow)
Spacer type	-	"Scenario" variable (void, overlapped, woven)
Spacer pitch-to-height ratio	P/H	2 (if a spacer is present)
Flow attack angle	φ	45° (if a spacer is present)
Absolute temperature	T	298.15 K, or 25°C
Areal Ohmic resistance of electrodes (per cell pair)	r_{blank}	5×10^{-5} Ω m^2
Singular pressure loss coefficients in manifolds	K^{CONC}, K^{DIL} (with $\Delta p=K\rho U_i^2/2$)	Both 10^4

b) Membrane properties (AMX-CMX Neosepta®)

Quantity	*Symbol*	*Reference values*
Thicknesses	H_{AEM}, H_{CEM}	134 and 158 μm, respectively
Perm-selectivities	α_{AEM}, α_{CEM}	0.9 and 0.95, respectively
Diffusive permeabilities	D_{AEM}, D_{CEM}	Both 5.5×10^{-11} m^2/s
Osmotic permeabilities	$L_{p,AEM}$, $L_{p,CEM}$	Both 1.38×10^{-14} m/(s·Pa), or 5 ml/(m^2·h·bar)
Areal Ohmic resistances	r_{AEM}, r_{CEM}	Concentration-dependent (see text)

In the following, the maximum of *NPD* is sought in the four-dimensional parameter space of H^{CONC}, H^{DIL}, U_i^{CONC}, U_i^{DIL} for different combinations of the remaining ("scenario") variables. Among these latter, in this study the inlet concentrations C_i^{CONC}, C_i^{DIL} were made to vary between 500 and 5000 mol/m^3 and between 5 and 100 mol/m^3, respectively, while the

stack length was made to vary between 0.1 and 1 m. Moreover, three distinct configurations were considered: void channels in parallel flow; woven spacer-filled channels in parallel flow; and woven spacer-filled channels in counter flow, so as to assess both the influence of spacers as opposed to the ideal case of void channels and the influence of counter- versus parallel-flow. On the whole, 6000 different combinations of "scenario" variables were examined.

All other quantities were kept fixed at the reference values indicated in Table 1. Membrane properties were representative of AMX/CMX Neosepta® membranes, as characterized in several studies [31, 32]. Ohmic resistances were provided by the correlation $r_{IEM} = a + b\left(C^{DIL}\right)^{-c}$ (Ω m^2) with a=2.8×10^{-4}, b=7×10^{-3}, c=1.25 (AMX) and a=2.5×10^{-4}, b=7×10^{-3}, c=1.25 (CMX) and C^{DIL} in mol/m^3.

3.2. Optimization algorithm

The gradient-ascent optimization algorithm adopted here is schematically illustrated in Figure 6 for the case of the search for the maximum of a function Ψ of two variables x_1, x_2. Starting from an arbitrary point A of coordinates x_i^A, the partial derivatives of Ψ (components of the gradient $\nabla\Psi$) are numerically approximated as

$$\frac{\partial \Psi}{\partial x_i} \approx \frac{\Psi(\mathbf{x}_A + \Delta x_i \mathbf{e}_i) - \Psi(\mathbf{x}_A - \Delta x_i \mathbf{e}_i)}{2\Delta x_i} \tag{29}$$

(in which Δx_i are small increments of the x_i and $\mathbf{e}_i$ are the basis vectors). The point A is then moved in small steps δ along the direction of the gradient

$$\mathbf{x}_A \rightarrow \mathbf{x}_A + \delta \nabla\Psi \tag{30}$$

until Ψ ceases to increase (say, up to point B). The gradient in B is then re-computed and the process starts again with a new segment BC. The search terminates when no further displacement of the representative point leads to an appreciable increase in Ψ (point F). The step δ was determined here as $C / \|\nabla\Psi\|$, in which $\|\nabla\Psi\|$ is the norm of the gradient:

$$\|\nabla\Psi\| = \sum \left(\frac{\partial \Psi}{\partial x_i} \right)^2 \tag{31}$$

while C is a dimensionless parameter, initially of order 1 and then reduced by a factor <1 at each new segment. Note that the gradient is recomputed only at a few points (as Eq. (29) shows, the computation of the gradient requires the evaluation of Ψ at 2n points, n being the number of variables, and thus can be quite time-consuming). The above algorithm was implemented in G95 Fortran®.

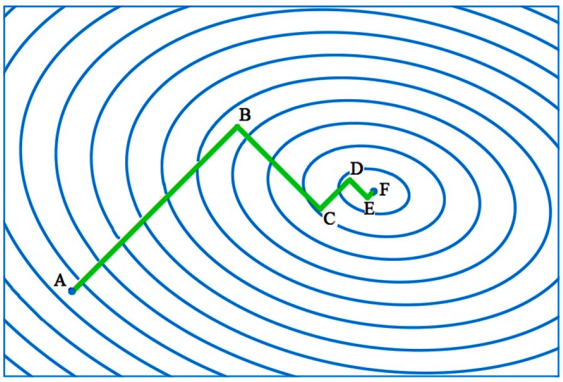

Figure 6. Illustration of the gradient-ascent optimization method for the case of 2 variables.

3.3. Results: spacerless channels in parallel flow

Figure 7 is for the ideal case of void (spacerless) channels in parallel flow. All quantities are reported as functions of the diluate concentration C_i^{DIL} for different concentrate concentrations C_i^{CONC} and a stack length L of 0.4 m.

Graphs (a) and (b) report the optimum channel thicknesses $H^{CONC}{}_{opt}$ and $H^{DIL}{}_{opt}$, respectively. The optimum thickness of the concentrate channel, graph (a), increases monotonically both with C_i^{CONC} and with C_i^{DIL} and varies quite significantly, from ~240 μm (C_i^{CONC}=500 mol/m^3, C_i^{DIL}=5 mol/m^3) to ~400 μm (C_i^{CONC}=5000 mol/m^3, C_i^{DIL}=100 mol/m^3). On the other hand, the optimum thickness of the diluate channel, graph (b), increases monotonically with C_i^{DIL} but decreases monotonically with C_i^{CONC}, varying from ~100 μm (C_i^{CONC}=5000 mol/m^3, C_i^{DIL}=5 mol/m^3) to ~200 μm (C_i^{CONC}=500 mol/m^3, C_i^{DIL}=100 mol/m^3). The optimum thickness of the diluate channel is always much less than that of the concentrate channel.

Graphs (c) and (d) report the optimum superficial inlet velocities $U_i^{CONC}{}_{opt}$ and $U_i^{DIL}{}_{opt}$, respectively. Both velocities increase monotonically with C_i^{CONC} and generally decrease with C_i^{DIL}, but some curves exhibit a shallow maximum for certain low values of this latter quantity. More specifically, $U_i^{CONC}{}_{opt}$ varies between ~1.5 cm/s (for C_i^{CONC}=500 mol/m^3, C_i^{DIL}=100 mol/m^3) and ~2.3 cm/s (for C_i^{CONC}=5000 mol/m^3, C_i^{DIL}=5 mol/m^3), while $U_i^{DIL}{}_{opt}$ varies between ~2.2 cm/s (for C_i^{CONC}=500 mol/m^3, C_i^{DIL}=100 mol/m^3) and ~6 cm/s (for C_i^{CONC}=5000 mol/m^3, $C_i^{DIL}\approx$15-20 mol/m^3). The optimum velocity in the diluate channel is always larger than that in the concentrate channel, a behaviour opposite to that discussed above for the optimum thickness.

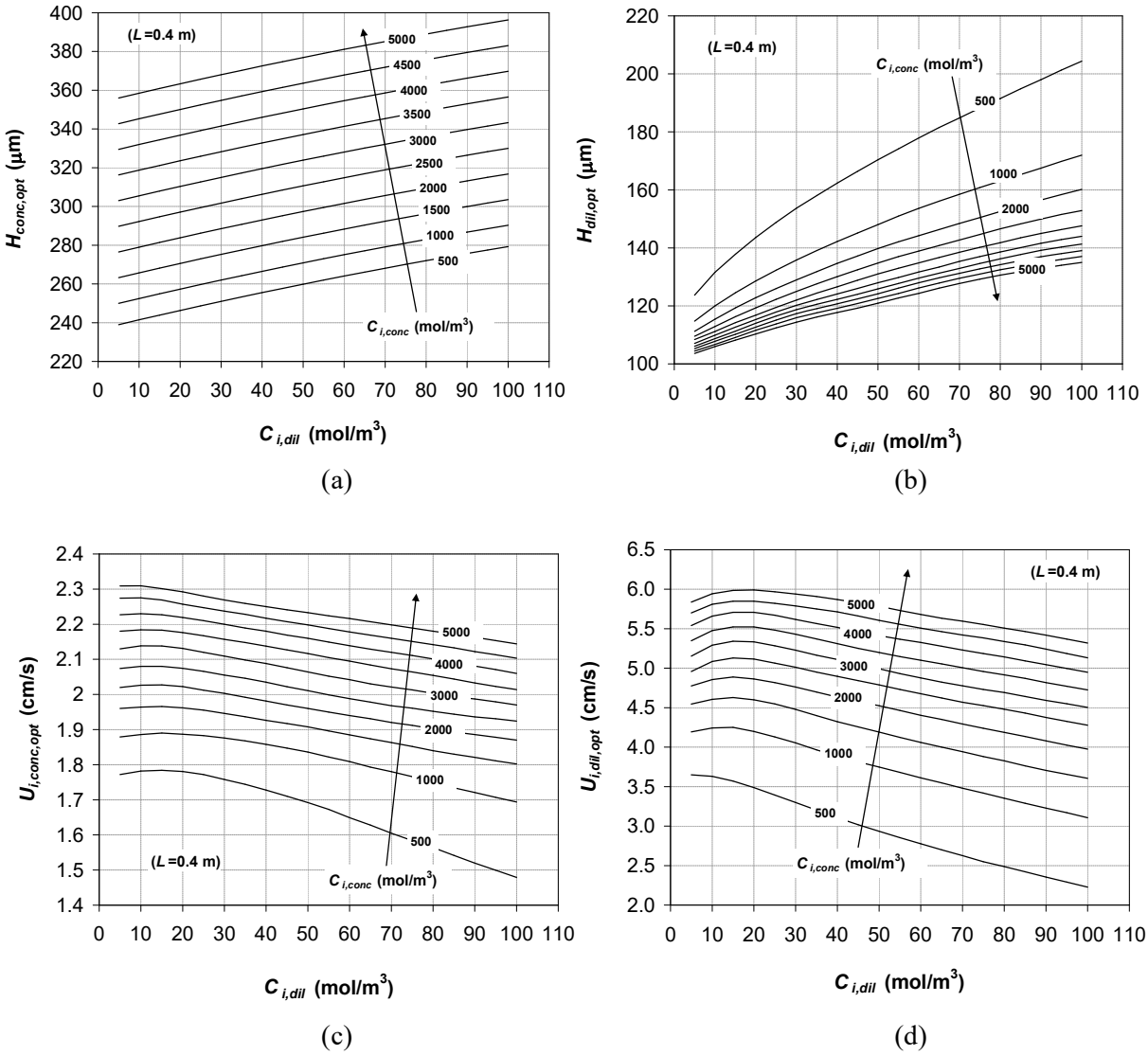

Figure 7. Results of the optimization study for spacerless channels in parallel flow. Graphs (a), (b), (c) and (d) show the values of H^{CONC}, H^{DIL}, U_i^{CONC}, U_i^{DIL}, respectively, providing the highest net power density *NPD*. All quantities are reported as functions of C_i^{DIL} for different values of C_i^{CONC} and L=0.4 m.

Figure 8(a) reports the net power density NPD_{opt} resulting from choosing the optimal values in Figure 7 for the channel thicknesses and flow velocities. NPD_{opt} increases monotonically with C_i^{CONC} but exhibits a shallow maximum as a function of C_i^{DIL} for very low values of this quantity. This is due to the fact that very low values of C_i^{DIL} act beneficially on the electromotive force E in Figure 3, but lead to high values of the diluate Ohmic resistance and thus of the Ohmic voltage drop η_Ω, which reduces power density. In the range considered, the highest value of NPD_{opt} (~7.7 W/m^2) is attained for the highest concentrate concentration (5000 mol/m^3, corresponding to a dense brine) and a diluate concentration of 15-20 mol/m^3 (typical river water).

By comparison, Figure 8(b) reports the net power density obtained by the choice of arbitrary, but typical, fixed reference values for the same parameters (H^{CONC}=H^{DIL}=200 μm, U_i^{CONC}=U_i^{DIL}=2 cm/s). It can be observed that in this case values of *NPD* (called here NPD_{ref}) are, in general, significantly lower; optimization leads to an increase in *NPD* that ranges from ~0 for the lowest $C_{i,conc}$ to ~25% for the highest $C_{i,conc}$. Optimization also leads to a larger sensitivity of *NPD* to both inlet concentrations.

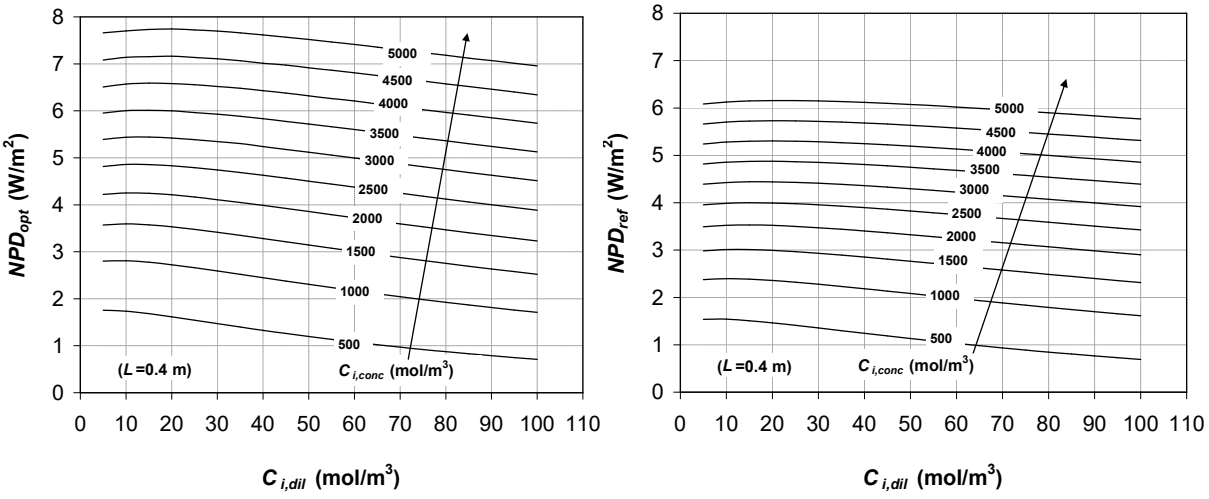

Figure 8. Spacerless channels in parallel flow: net power density *NPD* as a function of C_i^{DIL} for different values of C_i^{CONC} and L=0.4 m. (a): optimum values of H^{CONC}, H^{DIL}, U_i^{CONC}, U_i^{DIL}; (b): reference values of the same parameters (H^{CONC}=H^{DIL}=200 μm, U_i^{CONC}=U_i^{DIL}=2 cm/s).

3.4. Results: spacer-filled channels in parallel flow

Figure 9 reports the same quantities as Figure 7, but for channels filled with woven spacers having a pitch-to-height ratio P/H=2 and a flow attack angle φ=45°. The flow arrangement is still parallel as in Figure 7.

The values of the control parameters H^{CONC}, H^{DIL}, U_i^{CONC}, U_i^{DIL} corresponding to the *NPD* maximum, graphs (a)-(d), are much different than for void channels. In particular, $H^{CONC}{}_{opt}$ in graph (a) is now larger, ranging from ~350 to ~550 μm (according to C_i^{CONC} and C_i^{DIL}), and does not increase monotonically with C_i^{DIL} but exhibits a rather flat behaviour with respect to this parameter. Also $H^{DIL}{}_{opt}$ in graph (b) increases significantly with respect to the spacerless case, and now ranges from ~160 to ~290 μm. On the contrary, optimum flow velocities are now smaller than in spacerless channels. In particular, $U_i^{CONC}{}_{opt}$, graph (c), ranges now between ~1.1 and ~1.8 cm/s, with a 20-25% decrease with respect to the

spacerless case, and – like $H^{CONC}{}_{opt}$ – is less affected by C_i^{DIL}. $U_i^{DIL}{}_{opt}$, graph (f), now ranges between ~1.6 and ~4.4 cm/s, ~25% less than in the spacerless case.

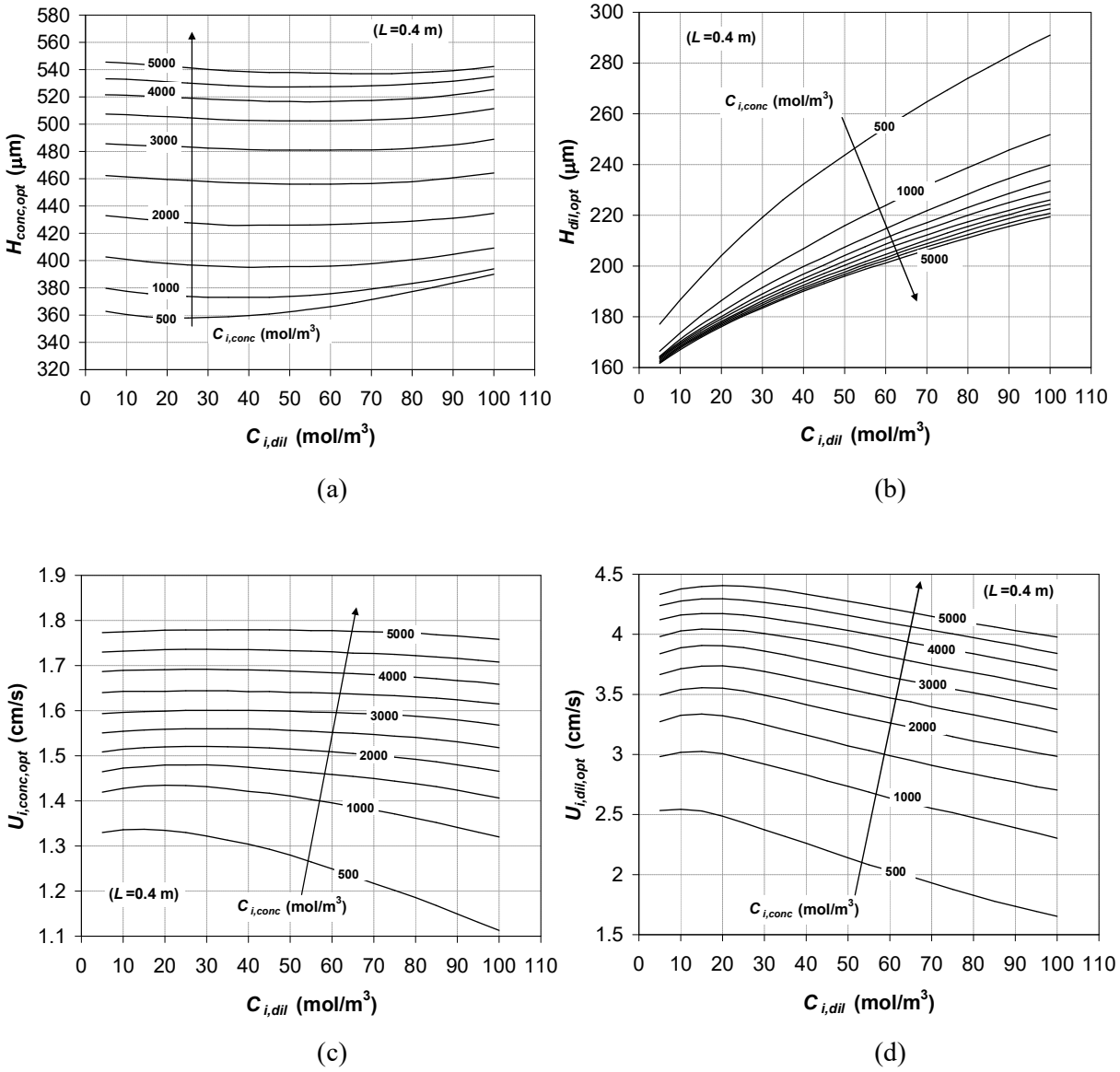

Figure 9. Results of the optimization study for channels filled by woven spacers (P/H=2, φ=45°) in parallel flow. Graphs (a), (b), (c) and (d) show the values of H^{CONC}, H^{DIL}, U_i^{CONC}, U_i^{DIL}, respectively, providing the highest net power density *NPD*. All quantities are reported as functions of C_i^{DIL} for different values of C_i^{CONC} and L=0.4 m.

The reason for the increase in optimum thicknesses and the corresponding decrease in optimum velocities is that spacers cause a large increase in the friction coefficient, putting a penalty on excessively high flow speeds or excessively thin channels *via* an increase in in pumping power density.

Values of NPD_{opt}, Figure 10(a), are not significantly different from those computed for

void channels; the highest value of NPD_{opt} rises from ~7.7 to ~8, and the overall dependence of NPD_{opt} on C_i^{CONC} and C_i^{DIL} is the same. The comparison with corresponding values of NPD_{ref}, Figure 10(b), shows that the benefits of optimization are similar to those observed for the spacerless case.

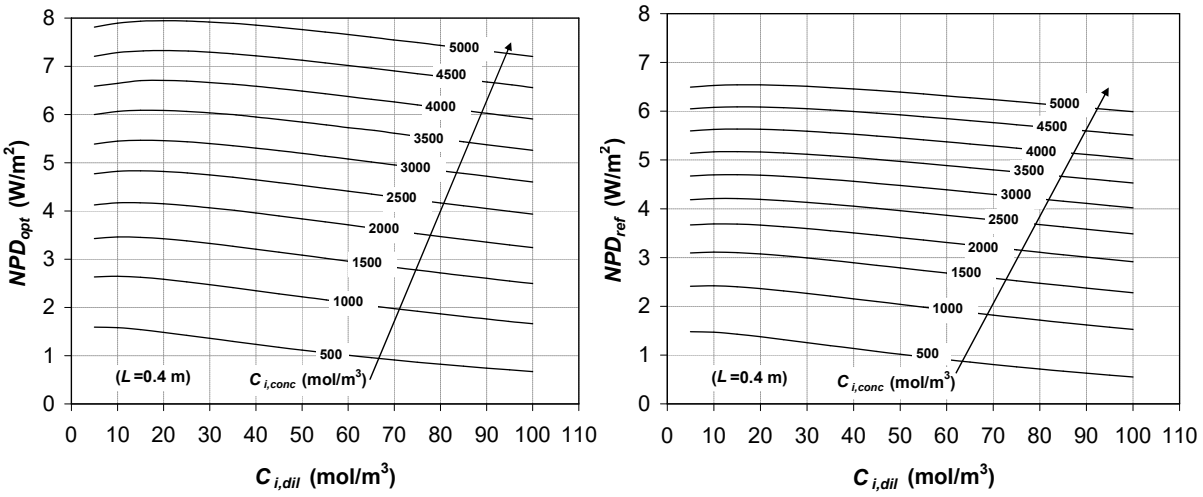

(a) (b)

Figure 10. Channels filled by woven spacers (P/H=2, φ=45°) in parallel flow: net power density NPD as a function of C_i^{DIL} for different values of C_i^{CONC} and L=0.4 m. (a): optimum values of H^{CONC}, H^{DIL}, U_i^{CONC}, U_i^{DIL}; (b): reference values of the same parameters (H^{CONC}=H^{DIL}=200 μm, U_i^{CONC}=U_i^{DIL}=2 cm/s).

For the present case of spacer-filled channels in parallel flow, which is the most likely to be encountered in practical applications, Figures 11-12 illustrate the influence of the stack length L.

In particular, Figure 11 reports optimum values of channel thickness and flow velocity as functions of L, in the range 0.1-1 m, for different concentrate concentrations C_i^{CONC} and a fixed diluate concentration C_i^{DIL}=15 mol/m^3. The optimal channel thicknesses H^{CONC}, H^{DIL}, graphs (a) and (b), both increase with L; for L=1 m, they become as high as 550 μm and 310 μm, respectively, when the concentrate is seawater ($C_{i,conc}$=500 mol/m^3), or 800 μm and 260 μm, respectively, when the concentrate is brine ($C_{i,conc}$=5000 mol/m^3). Note that, as already observed in discussing the results in Figure 7, $H^{CONC}{}_{opt}$ increases with $C_{i,conc}$ while $H^{DIL}{}_{opt}$ decreases. Graphs (c) and (d) show that also the optimal flow velocities both increase with L (despite the increase in frictional losses) because a high NPD is associated with a short residence time.

The results for the other configurations (void channels in parallel flow and spacer-filled channels in counter flow) are qualitatively similar.

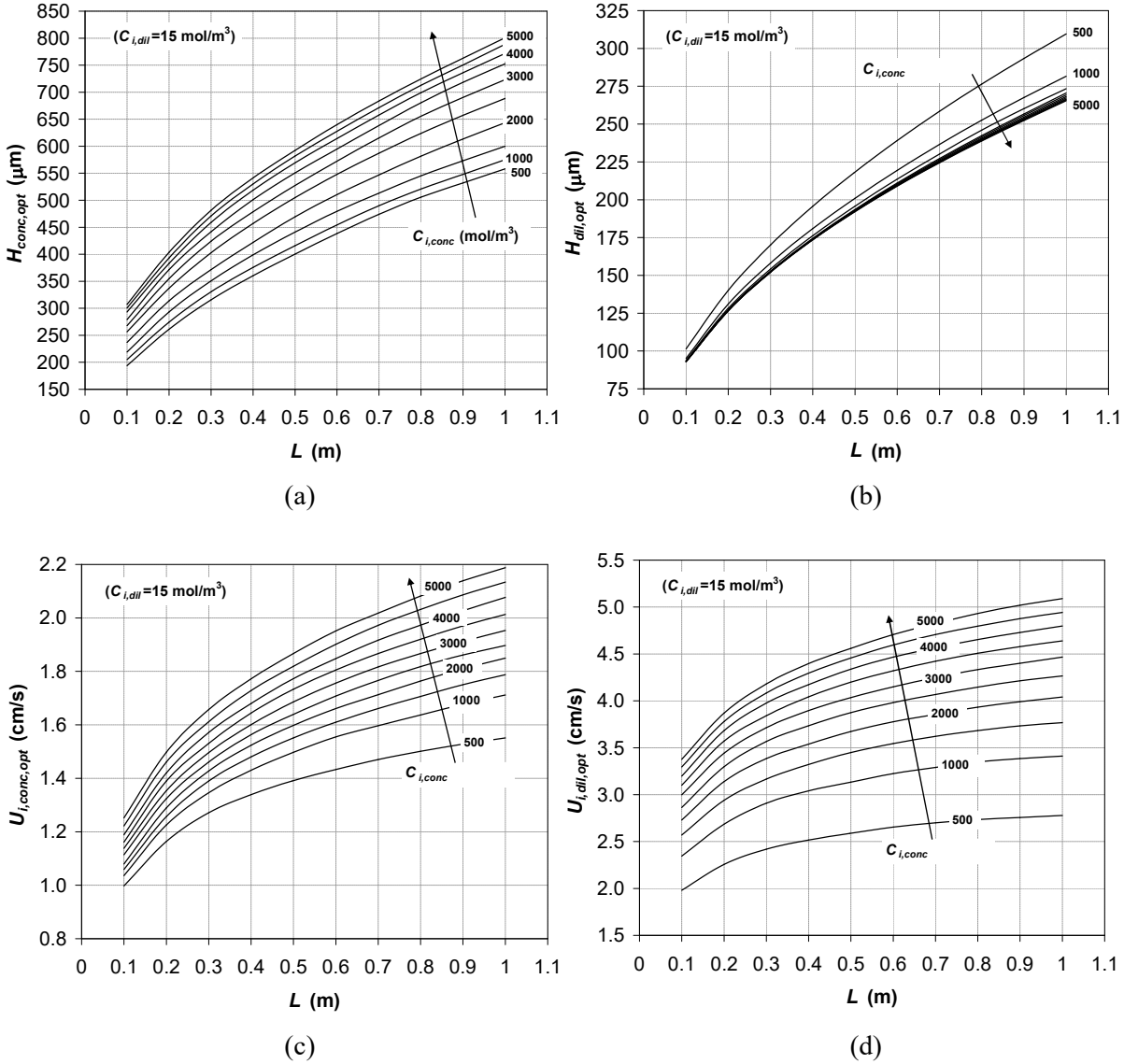

Figure 11. Results of the optimization study for channels filled by woven spacers (P/H=2, φ=45°) in parallel flow. Graphs (a), (b), (c) and (d) show the values of H^{CONC}, H^{DIL}, U_i^{CONC}, U_i^{DIL}, respectively, providing the highest net power density *NPD*. All quantities are reported as functions of the stack length L for different values of C_i^{CONC} and C_i^{DIL}=15 mol/m^3.

Figure 12 compares the values of *NPD* corresponding to the optimum choice of the parameters H^{CONC}, H^{DIL}, U_i^{CONC}, U_i^{DIL} (NPD_{opt}, graph (a)) with those corresponding to fixed reference values of the same parameters (NPD_{ref}, graph (b)). As in Figure 11, quantities are reported as functions of the stack length L (from 0.1 to 1 m) for varying $C_{i,conc}$ and a given value (15 mol/m^3) of $C_{i,dil}$.

The adverse influence of L on NPD can be observed. For example, for C_i^{CONC}=5000 mol/m^3 and the given C_i^{DIL}, a short stack with L=0.1 m yields NPD_{opt}≈10 W/m^2, while this quantity falls to ~6.5 W/m^2 when L=1 m. The comparison of graphs (a) and (b) shows that the benefits of optimization increase with increasing stack length; for L=1 m, the relative increase in NPD is larger than 50% for all values of $C_{i,conc}$. These improvements would be even more marked at higher diluate concentrations.

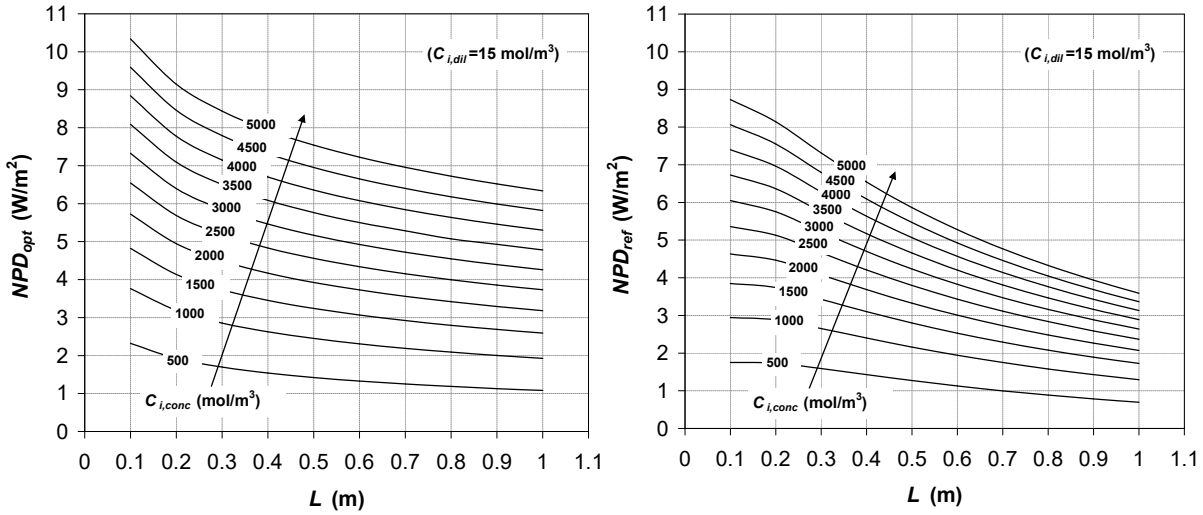

Figure 12. Channels filled by woven spacers (P/H=2, φ=45°) in parallel flow: net power density NPD as a function of the stack length L for different values of C_i^{CONC} and C_i^{DIL}=15 mol/m^3. (a): optimum values of H^{CONC}, H^{DIL}, U_i^{CONC}, U_i^{DIL}; (b): reference values of the same parameters (H^{CONC}=H^{DIL}=200 μm, U_i^{CONC}=U_i^{DIL}=2 cm/s).

It should be observed that the parameters providing the maximum net power density do *not* also provide optimum values of the electrical energy extracted from a given total volume of solutions (concentrate+diluate), or net energy density (NED).

Still for the case of channels filled by woven spacers and parallel flow, Figure 13 reports the quantity NED as obtained in correspondence either with the parameters H^{CONC}, H^{DIL}, U_i^{CONC}, U_i^{DIL} providing the highest NPD, graph (a) (NED_{opt}), or with fixed reference values of the same parameters, graph (b) (NED_{ref}). It can be observed that the optimization of NPD causes a reduction in NED ranging from a few percent for low values of $C_{i,conc}$ (e.g. 500 mol/m^3, i.e. seawater) to 40-50% for high values of $C_{i,conc}$ (e.g. 5000 mol/m^3, i.e. concentrated brine). This is mainly due to the lower residence times required for maximising NPD, compared to what would be needed in order to extract larger amount of energy from a specific

volume of feed solutions. The couple seawater-riverwater (C_i^{CONC}=500 mol/m^3, C_i^{DIL}=15 mol/m^3) gave $NED \approx 60$ kJ/m^3 for all stack lengths investigated (0.1-1 m) when *NPD* attained its maximum of ~1.1-2.2 W/m^2 (depending on the stack length). This *NED* is much lower than the theoretical maximum free energy of the solutions (~880 kJ/m^3 assuming equal amounts of concentrate and diluate [1]), and also lower than that obtained in stacks which were specifically optimized for *NED* (~100-200 kJ/m^3 [1]).

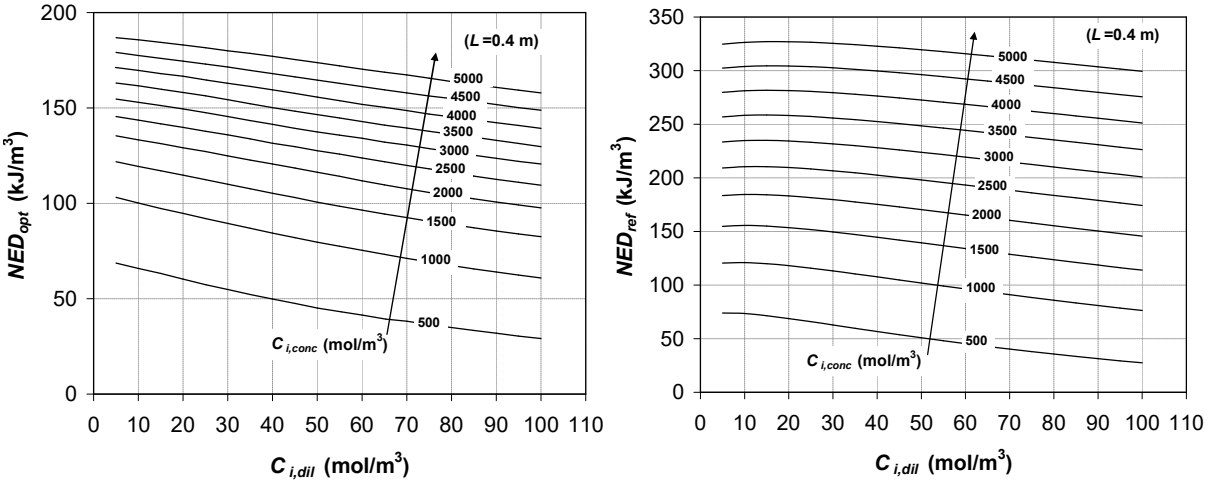

(a) (b)

Figure 13. Channels filled by woven spacers (P/H=2, φ=45°) in parallel flow: net energy density *NED* as a function of C_i^{DIL} for different values of C_i^{CONC} and L=0.4 m. (a): values of H^{CONC}, H^{DIL}, U_i^{CONC}, U_i^{DIL} chosen to maximize *NPD*; (b): reference values of the same parameters (H^{CONC}=H^{DIL}=200 μm, U_i^{CONC}=U_i^{DIL}=2 cm/s).

3.5. Results: spacer-filled channels in counter flow

Figures 14-15 reports the same quantities as Figures 7-8 and 9-10, but for woven spacer-filled channels in *counter* flow. By comparing Figure 14 with Figure 9, one may observe that optimum values of the parameters H^{CONC}, H^{DIL}, U_i^{CONC}, U_i^{DIL} are significantly different in counter flow than in parallel flow. In particular, switching from parallel to counter flow both $H^{CONC}{}_{opt}$ and $H^{DIL}{}_{opt}$ decrease by ~15-25% (according to the values of the "scenario" variables), and also optimum flow velocities decrease, although to a lesser extent (~5-15%).

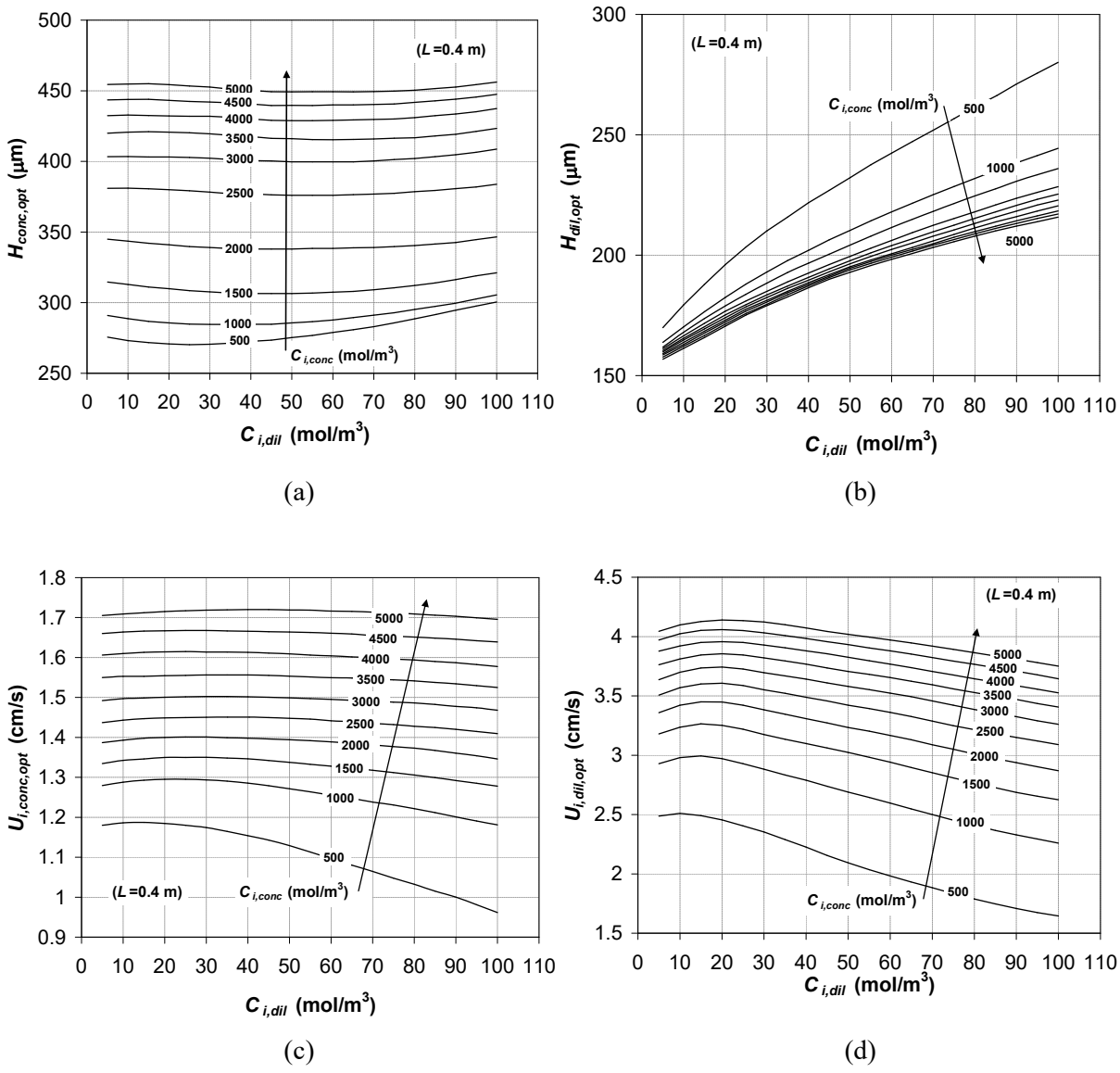

Figure 14. Results of the optimization study for channels filled by woven spacers (P/H=2, φ=45°) in counter flow. Graphs (a), (b), (c) and (d) show the values of H^{CONC}, H^{DIL}, U_i^{CONC}, U_i^{DIL}, respectively, providing the highest net power density *NPD*. All quantities are reported as functions of C_i^{DIL} for different values of C_i^{CONC} and L=0.4 m.

On the other hand, the comparison of Figure 15 with Figure 10 shows that the resulting values of NPD_{opt} are very similar, with only a very small increase with respect to parallel flow. This is mainly due to the weak dependence of *NPD* on the optimization variables.

Also for the present case of woven spacers in counter-flow, graphs of the net energy density *NED* corresponding to the choice of optimization variables that maximizes *NPD* (NED_{opt}) and to fixed, reference values of the same variables (NED_{ref}), show a behaviour similar to that discussed for woven spacers and parallel flow, i.e., a strong reduction of *NED* in correspondence with the optimization of *NPD*, and were not reported for brevity.

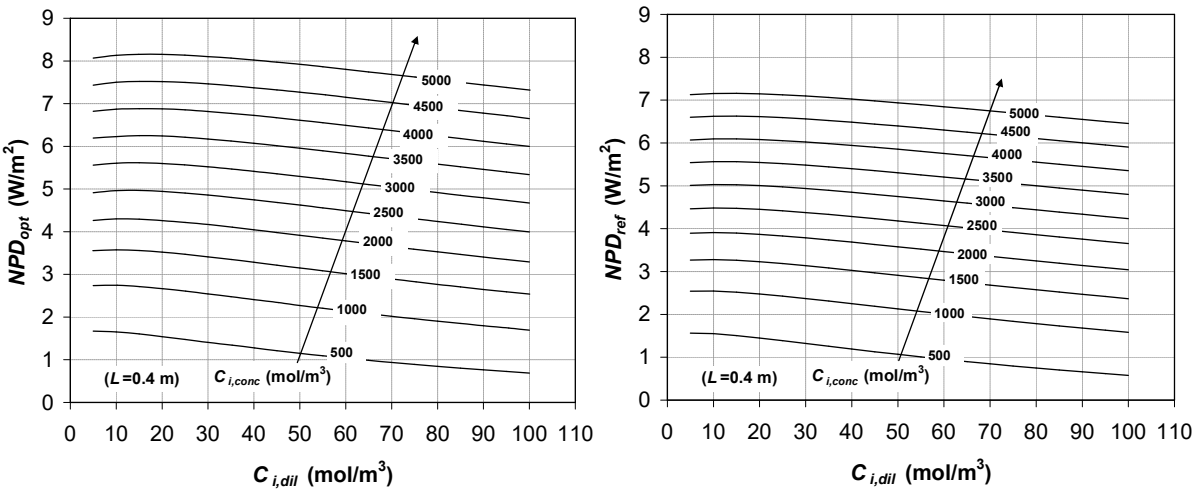

(a) (b)

Figure 15. Channels filled by woven spacers (P/H=2, φ=45°) in counter flow: net power density NPD as a function of C_i^{DIL} for different values of C_i^{CONC} and L=0.4 m. (a): optimized values of H^{CONC}, H^{DIL}, U_i^{CONC}, U_i^{DIL}; (b): reference values of the same parameters (H^{CONC}=H^{DIL}=200 μm, U_i^{CONC}=U_i^{DIL}=2 cm/s).

4. Conclusions

A simplified model of a RED stack was coupled with an optimization algorithm to determine the conditions for maximum net power density (NPD) in the parameter space H^{CONC}, H^{DIL},U^{CONC}, U^{DIL} for different combinations of the remaining ("scenario") variables.

The thicknesses and flow velocities in the channels yielding maximum values of NPD were found to be sensitive to "scenario" variables such as inlet concentrations and stack length. Both in spacerless and in spacer-filled channel, the optimum thickness of the concentrate channels was found to increase with the concentrate solution concentration and with the stack length, while being less sensitive to the dilute solution concentration. The optimum thickness of the diluate channels was found to decrease with the concentrate concentration while increasing with the diluate concentration and with the stack length. The optimum velocities both in the concentrate and in the diluate channels were found to increase markedly with the concentrate concentration and with the stack length and to exhibit a generally decreasing trend with the diluate concentration, with some local maxima for low values of this quantity (~10-20 mol/m^3). The optimum thickness of the concentrate channels was found to be from two to three times higher than that of the diluate channels, while the optimum velocity in the concentrate channels was found to be two-three times lower than that

in the diluate ones. The resulting optimum *NPD* was found to increase monotonically with the concentrate concentration, to exhibit shallow maxima for diluate concentrations of 10-20 mol/m^3, and to decrease with the stack length. Interestingly, the flow rates corresponding to maximum *NPD* were found to be comparable under all conditions investigated, their ratio (concentrate/diluate) ranging from ~0.85 to ~1.3 in most cases.

Under conditions maximizing the net power density, the net energy density *NED* (electrical power output divided by the volumetric flow rate of concentrate and diluate) was generally lower than in the case of an arbitrary and fixed choice of channel thicknesses and solution velocities (especially at high concentrate concentrations), showing that *NPD* can be maximized only at the cost of a less efficient utilization of the feed solutions.

The comparison of spacerless and spacer-filled channels showed that these latter do not significantly affect *NPD*, but cause drastic changes in the optimum values of the control parameters: namely, a strong increase in the optimum thickness of both concentrate and diluate channels, and a comparable decrease in the optimum velocities of both channels. The comparison of parallel- and counter-flow showed that in counter-flow the maximum *NPD* increases only slightly, but the optimum thicknesses and – to a lesser extent – the optimum flow velocities in both channels decrease significantly. Under common seawater-riverwater conditions, some of the quantities investigated exhibit optimum values significantly different from the values currently adopted in lab-scale and prototype stacks; for example, the optimum thickness of the concentrate channels in parallel flow is more than 350 μm and the flow velocity in the diluate channels, both in parallel- and in counter-flow, is ~2.5 cm/s.

Needless to say, the above results were based on some, rather arbitrary, assumptions, the most relevant being the independence of membrane perm-selectivities α upon the solution concentrations and the modelling of off-channel pressure losses by means of constant hydraulic loss coefficients. In future work, these assumptions will be replaced by more realistic models. Another possible extension of this study would be the optimization of a suitable target function, combining net power density, net energy density and plant cost, rather than of the single quantity *NPD*.

Acknowledgements

This work was performed within the RED-Heat-to-Power (Conversion of Low Grade Heat to Power through closed loop Reverse Electro-Dialysis) project, Horizon 2020 programme, Grant Agreement no. 640667 (www.red-heat-to-power.eu).

Nomenclature

Symbol	*Quantity*	*Unit*
a, b, c	Constants in membrane resistance	various
C	Bulk concentration	mol m^{-3}
D_{IEM}	Salt diffusive permeability in membrane	m^2 s^{-1}
E	Electromotive force per cell pair	V
$\mathbf{e}_i$	Basis vectors in parameter space	-
F	Faraday's constant, 9.6485×10^4	C mol^{-1}
f	Darcy friction coefficient	-
GPD	Gross power density per cell pair	W m^{-2}
H	Thickness (channel, membrane, cell pair)	m
I	Electrical current	A
i	Electrical current density	A m^{-2}
K	Singular pressure loss coefficient	-
L	Stack length	m
L_p	Osmotic permeability	m s^{-1} Pa^{-1}
n	Generic number	-
n_H	Hydration number	-
NED	Net energy per unit volume of solutions	J m^{-3}
NPD	Net power density per cell pair	W m^{-2}
P	Pitch of spacers	m
PPD	Pumping power density per cell pair	W m^{-2}
R_G	Gas constant, 8.3415	J mol^{-1} K^{-1}
R	Electrical resistance	Ω
r	Areal electrical resistance	Ω m^2
S	Projected surface area of stack, LW	m^2
T	Absolute temperature	K
U	Superficial velocity, $Q/(HW)$	m s^{-1}
V	Overall voltage drop in stack	V
v	Voltage drop per cell pair	V
W	Stack width (spanwise extent)	m
x_i	Generic variables in parameter space	various
y	Co-ordinate along the flow direction	m

Greek symbols

α	Membrane permselectivity	-
Δp	Pressure drop	Pa
δ	Increment in gradient ascent algorithm	various
η	Electrical voltage drop per cell pair	V
φ	Flow attack angle	deg
Ψ	Generic target function to be maximized	-

Subscripts

AEM	Anion Exchange Membrane
BL	Related to concentration boundary layer
blank	Pertaining to electrode compartments
CEM	Cation Exchange Membrane
cp	Cell pair
IEM	Ion exchange membrane (*AEM*/*CEM*)
i	Inlet
LOAD	External electrical load
opt	Optimized
P	Working point
ref	Reference
S	Short circuit
ΔC	Related to axial changes in concentration
Ω	Ohmic
∞	Infinite length

Superscripts

CONC	Concentrated solution
DIL	Dilute solution

Averages

$\langle\ \rangle$	Over the stack length or projected surface

References

1. Veerman J, Saakes M, Metz SJ, Harmsen GJ. Reverse electrodialysis: Performance of a stack with 50 cells on the mixing of sea and river water. J Membr Sci 2009;327:136–144.
2. Wick GL. Power from salinity gradients. Energy 1978;3:95–100.
3. Tedesco M, Cipollina A, Tamburini A, Micale G. Towards 1 kW power production in a reverse electrodialysis pilot plant with saline waters and concentrated brines. J Membr Sci 2017;522:226–36.
4. Vermaas DA, Saakes M, Nijmeijer K. Power generation using profiled membranes in reverse electrodialysis. J Membr Sci 2011;385–386:234–42.
5. Gurreri L, Ciofalo M, Cipollina A, Tamburini A, Van Baak W, Micale G. CFD modelling of profiled-membrane channels for reverse electrodialysis. Desalin Water Treat 2015;55:1–20.
6. Gurreri L, Battaglia G, Tamburini A, Cipollina A, Micale G, Ciofalo M. Multi-physical modelling of reverse electrodialysis. Desalination 2017;423:52–64.
7. Scialdone O, Guarisco C, Grispo S, D'Angelo A, Galia A. Investigation of electrode material – Redox couple systems for reverse electrodialysis processes. Part I: Iron redox couples. J Electroanal Chem 2012;681:66–75.
8. Vermaas DA, Guler E, Saakes M, Nijmeijer K. Theoretical power density from salinity gradients using reverse electrodialysis. Energy Procedia 2012;20:170–84.
9. Daniilidis A, Vermaas DA, Herber R, Nijmeijer N. Experimentally obtainable energy from mixing river water, seawater or brines with reverse electrodialysis. Renew Energy 2014;64:123–31.
10. La Cerva M, Di Liberto M, Gurreri L, Tamburini A, Cipollina A, Micale G, Ciofalo M. Coupling CFD with simplified 1-D models to predict the performance of Reverse Electrodialysis stacks. J Membr Sci 2017;541:596–610.
11. Post JW, Hamelers HVM, Buisman CJN. Energy recovery from controlled mixing salt and fresh water with a reverse electrodialysis system. Envir Sci Technol 2008;42:5785–90.
12. Cipollina A, Micale G, Tamburini A, Tedesco M, Gurreri L, Veerman J, Grasman S. Reverse electrodialysis: Applications. In: Cipollina A, Micale G, editors. Sustainable Energy from Salinity Gradients, Amsterdam: Elsevier Inc; 2016, p. 135–80.
13. Strathmann H. Ion-exchange membrane separation processes. 1st ed. Amsterdam: Elsevier; 2004.

14. Tedesco M, Cipollina A, Tamburini A, Bogle IDL, Micale G. A simulation tool for analysis and design of reverse electrodialysis using concentrated brines. Chem Eng Res Des 2015;93:441−56.
15. Vermaas DA, Saakes M, Nijmeijer K. Doubled power density from salinity gradients at reduced intermembrane distance. Environ Sci Technol 2011;45:7089−95.
16. Długołęcki P, Gambier A, Nijmeijer K, Wessling M. Practical potential of reverse electrodialysis as process for sustainable energy generation. Environ Sci Technol 2009;43:6888−94.
17. Gurreri L, Tamburini A, Cipollina A, Micale G, Ciofalo M. CFD prediction of concentration polarization phenomena in spacer-filled channels for reverse electrodialysis. J Membr Sci 2014;468:133−48.
18. Vermaas DA, Saakes M, Nijmeijer K. Enhanced mixing in the diffusive boundary layer for energy generation in reverse electrodialysis. J Membr Sci 2014;453:312−19.
19. Pawlowski S, Sistat P, Crespo JG, Velizarov S. Mass transfer in reverse electrodialysis: Flow entrance effects and diffusion boundary layer thickness. J Membr Sci 2014;471:72−83.
20. Avci AH, Tufa RA, Fontananova E, Di Profio G, Curcio E. Reverse Electrodialysis for energy production from natural river water and seawater. Energy 2018;165:512−21.
21. Gurreri L, Tamburini A, Cipollina A, Micale G, Ciofalo M. Pressure drop at low Reynolds numbers in woven-spacer-filled channels for membrane processes: CFD prediction and experimental validation. Desalin Water Treat 2017;61:170−82.
22. Veerman J, Saakes M, Metz SJ, Harmsen GJ. Reverse electrodialysis: a validated process model for design and optimization. Chem Eng J 2011;166:256−68.
23. Vallejo-Castaño S, Sánchez-Sáenz CI. Design and optimization of a reverse electrodialysis stack for energy generation through salinity gradients. Dyna 2017;84:84−91.
24. Long R, Li B, Liu Z, Liu W. Reverse electrodialysis: modelling and performance analysis based on multi-objective optimization. Energy 2018;151:1−10.
25. Long R, Li B, Liu Z, Liu W. Performance analysis of reverse electrodialysis stacks: Channel geometry and flow rate optimization. Energy 2018;158:427−36.
26. Tamburini A, Cipollina A, Tedesco M, Gurreri L, Ciofalo M, Micale G, The REAPower project: power production from saline waters and concentrated brines. In: Basile A, Curcio E, Inamuddin D, editors. Current Trends and Future Developments on (Bio-) Membranes, Amsterdam: Elsevier Inc; 2018, p. 407−48.

27. Bevacqua M, Tamburini A, Papapetrou M, Cipollina A, Micale G, Piacentino A, Reverse electrodialysis with NH_4HCO_3-water systems for heat-to-power conversion, Energy 2017;137:1293−307.
28. Giacalone F, Olkis C, Santori G, Cipollina A, Brandani S, Micale G. Novel solutions for closed-loop reverse electrodialysis: Thermodynamic characterization and perspective analysis. Energy 2018;166:674−89.
29. Pawlowski S, Geraldes V, Crespo JG, Velizarov S. Computational fluid dynamics (CFD) assisted analysis of profiled membranes performance in reverse electrodialysis. J Membr Sci 2016;502:179−90.
30. Choi I, Han JY, Yoo SJ, Henkensmeier D, Kim JY, Lee SY, Han J, Nam S.W, Kim H-J, Jang JH. Experimental Investigation of Operating Parameters in Power Generation by Lab-Scale Reverse Electro-Dialysis (RED). Bull Korean Chem Soc 2016;37:1010−19.
31. Galama AH, Hoog NA, Yntema DR. Method for determining ion exchange membrane resistance for electrodialysis systems. Desalination 2016;380:1−11.
32. Veerman J, de Jong RM, Saakes M, Metz SJ, Harmsen GJ, Reverse electrodialysis: Comparison of six commercial membrane pairs on the thermodynamic efficiency and power density. J Membr Sci 2009;343:7−15.